

Detection of topological matter with quantum gases

Ian B. Spielman*

Received 12 May 2013, revised 10 June 2013, accepted 20 June 2013

Published online 1 August 2013

Creating and measuring topological matter – with non-local order deeply embedded in the global structure of its quantum mechanical eigenstates – presents unique experimental challenges. Since this order has no signature in local correlation functions, it might seem experimentally inaccessible in any macroscopic system; however, as the precisely quantized Hall plateaux in integer and fractional quantum Hall systems show, topology can have macroscopic signatures at the system's edges. Ultracold atoms provide new experimental platforms where both the intrinsic topology and the edge behavior can be directly measured. This article reviews, using specific examples, how non-interacting topological matter may be created and measured in quantum gases.

1 Introduction

Measurement. Science is rooted in measurement: it is from measurements, as unified by theory, that understanding is born. Our comprehension of the universe is therefore bounded by our ability to observe and shaped by human creativity. Scientific progress is driven by the identification of new physical systems and measurement techniques, leading to new conceptual understanding. This article focuses on systems of ultracold neutral atoms, quantum gases, that make quantum physics manifest in the laboratory. Many properties of these systems can be understood in the intellectual context of many-body physics which describes systems from the commonplace, such as crystals, fluids, and semiconductors, to the extreme, such as superconductors, quantum Hall systems, and neutron stars. Many-body physics asks how the properties of individual components – atoms, electrons, nucleons – give rise to the observed macroscopic phenomena. For example, classifying phases of matter and understanding the transitions between them is an essential part of condensed matter physics.

Matter, with all its myriad phases, surrounds us. Some phases are familiar, such as gases, liquids, or even ferromagnets, while others, such as antiferromagnets or nematics, are still ubiquitous but pass us by, quite unknown to our everyday existence. Each of these phases is characterized by a local order parameter that captures the type and degree of order associated with it. For example, the ferromagnetic order parameter is simply the local degree of magnetization and the superfluid order parameter is the (complex-valued) superfluid density. Microscopically, these phases of matter result from the complicated interaction between practically uncountable many elementary constituents, yet their basic physics can be encapsulated in reduced models that include only those degrees of freedom which are important to a specific phase or phase transition.

Unlike ferromagnets, antiferromagnets are difficult to identify macroscopically, though their local order parameters are almost the same: magnetization compared to staggered magnetization. While staggered magnetic order might be “hidden” from our daily existence, neutron scattering makes it easy to identify [1].

Quite in contrast, a new type of order first known in the B-phase [2, 3] of superfluid ^3He and then found in the integer quantum Hall states [4, 5] in two-dimensional (2D) electron systems is hidden in a more fundamental way. This *topological* order cannot be described by any local order parameter; instead, topological order is encapsulated by global topological invariants such as Chern numbers or Z_2 invariants [6]. With the discovery of topological insulators [7] – zero-magnetic-field analogs to integer quantum Hall effects (IQHEs) that preserve time-reversal (TR) symmetry – interest in topological order has been rekindled, leading finally to a complete classification of topological insulators (TIs) and superconductors [6] (only some of which exist in current material systems [7], such as HgCdTe quantum wells or bulk Bi_2Se_3).

* Corresponding author E-mail: ian.spielman@nist.gov
Joint Quantum Institute, National Institute of Standards and Technology, and University of Maryland, Gaithersburg, MD, 20899, USA

Ultracold atoms are very different from conventional materials, composed of a few [8] to a few hundred million atoms [9], with densities ranging from below 10^{12} cm^{-3} up to approximately 10^{15} cm^{-3} , and at temperatures from below 1 nK to a couple of microkelvins. These atomic systems are unique in the simplicity of their underlying Hamiltonians along with remarkable experimental flexibility, enabling experimentalists to control and engineer their quantum degrees of freedom. An almost unavoidable requirement for creating topological matter is the existence of static gauge fields in the microscopic Hamiltonian. Examples include the electromagnetic vector potential describing a large magnetic field in the case of quantum Hall systems, or spin–orbit couplings for TR invariant TIs. This article assumes the existence of these fields, and focuses on detecting the resulting phases of matter.

For a broad overview of artificial gauge fields, I refer the interested reader to one of several high-quality contemporary reviews or book chapters, either at a high level [10], or with a more technical focus [11–13]. In light of those reviews, this article will focus on a couple of specific examples of how ultracold atom systems can realize topological matter, and how the unique measurement opportunities thereby afforded open new windows into these systems. Topological matter can be manifested either by its transport properties – as is typically observed in condensed matter systems – or more directly by topological properties of the eigenstates. Measurement of both is possible with cold atoms.

2 Light–matter interaction

First, if artificial gauge fields are to be created using internal – spin – atomic degrees of freedom coupled by light, then we must understand the basic spin-dependent interaction between light and matter. The conventional spin-independent (scalar, U_s) optical potentials acquire additional spin-dependent terms near atomic resonances [14–16]: the rank-1 (vector, U_v) and rank-2 tensor light shifts. For the alkali metal atoms illuminated by light near the $j = 1/2$ (D1) and $j = 3/2$ (D2) lines, the effective atom–light coupling Hamiltonian for the ground-state atoms (with $j = 1/2$) is

$$H_L = \left[u_s(\mathbf{E}^* \cdot \mathbf{E}) + \frac{i u_v(\mathbf{E}^* \times \mathbf{E})}{\hbar} \cdot \mathbf{j} \right],$$

where \mathbf{E} is the complex-valued optical electric field. The rank-2 term is negligible for the parameters of interest and hence is not included in H_L . Here $u_v =$

$-2u_s \Delta_{FS}/3(\omega - \omega_0)$ determines the vector light shift; $\Delta_{FS} = \omega_{3/2} - \omega_{1/2}$ is the fine-structure splitting; $\hbar\omega_{1/2}$ and $\hbar\omega_{3/2}$ are the D1 and D2 transition energies; and $\omega_0 = (2\omega_{1/2} + \omega_{3/2})/3$ is a suitable average. u_s sets the scale of the light shift and is proportional to the atoms' AC polarizability.

The scalar and vector light shifts in H_L can be independently specified with informed choices of laser frequency ω and intensity. Evidently, the vector light shift is a contribution to the total Hamiltonian acting like an effective magnetic field

$$\mathbf{B}_{\text{eff}} = \frac{i u_v(\mathbf{E}^* \times \mathbf{E})}{\mu_B g_J}$$

that acts on \mathbf{j} and not the nuclear spin \mathbf{I} . At small magnetic fields when the Zeeman shifts are small in comparison with the hyperfine splitting – the linear, or anomalous, Zeeman regime – the effective Hamiltonian for a single manifold of total angular momentum $\mathbf{F} = \mathbf{j} + \mathbf{I}$ states is

$$H_0 + H_L = u_s(\mathbf{E}^* \cdot \mathbf{E}) + \frac{\mu_B g_F}{\hbar} (\mathbf{B} + \mathbf{B}_{\text{eff}}) \cdot \mathbf{F} + \frac{A_{\text{hf}}}{2} (\mathbf{F}^2 - \mathbf{j}^2 - \mathbf{I}^2).$$

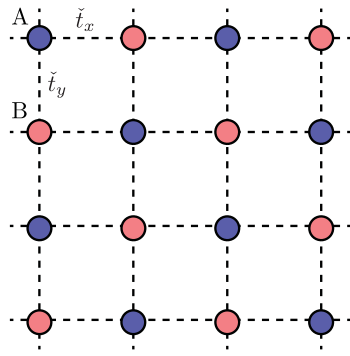
Here \mathbf{B}_{eff} acts as a true magnetic field and adds vectorially with \mathbf{B} , and since $|g_I/g_J| \simeq 0.0005$ in alkali metal atoms, we safely neglected a contribution $-\mu_B g_I \mathbf{B}_{\text{eff}} \cdot \mathbf{I}/\hbar$ to the Hamiltonian. We also introduced the hyperfine Landé g-factor $g_F = g_J[f(f+1) - i(i+1) + j(j+1)]/[2f(f+1)]$. In the lowest energy manifold of ^{87}Rb with $f = 1$, for which $j = 1/2$ and $i = 3/2$, we get $g_F = -g_J/4 \approx -1/2$.

3 Basic concepts and direct measurement

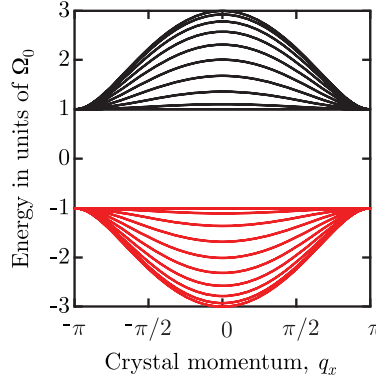
Ultracold atomic systems are unique in their simplicity, allowing for the direct experimental measurement of specific physical phenomena uncomplicated by spurious effects. For example, particles moving in a 2D lattice potential are described in terms of a series of energy bands $E_n(\mathbf{q})$, where \mathbf{q} is the crystal momentum. Each of these bands, labeled by index n , is associated with a Chern number C_n , an integer characterizing its topological properties. To better understand this characterization of energy bands, we will consider a simple model of a spin-1/2 particle with band structure given by the Hamiltonian density

$$\check{H}(\mathbf{q}) = \left[\frac{1}{2} \Omega(\mathbf{q}) \cdot \check{\sigma}_{mn} \right] \hat{\phi}_m^\dagger(\mathbf{q}) \hat{\phi}_n(\mathbf{q}),$$

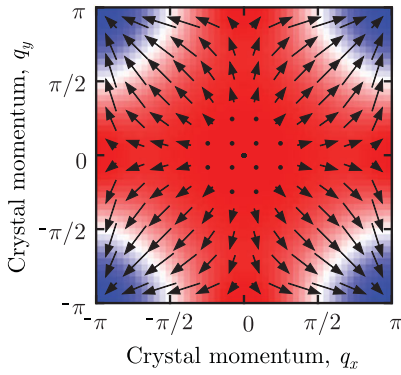
(a) Lattice schematic



(b) Band structure



(c) Spin orientation



(d) Chern number

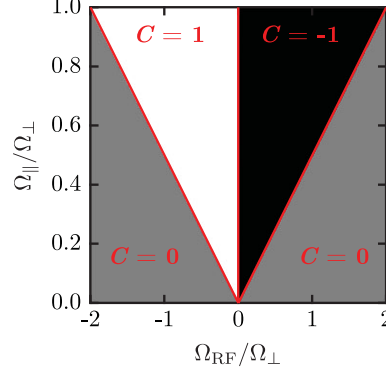


Figure 1 Topological square lattice. (a) Lattice topology showing the A and B sites coupled with spin-dependent light- or radiofrequency-induced “Raman” hopping. (b) Band structure depicting slices taken at different values of q_y , computed for $\Omega_0 = \Omega_{\parallel} = \Omega_{\perp} = \Omega_{\text{RF}}$. (c) Orientation of the eigenstate spin vector $\mathbf{n}(\mathbf{q})$ on the Bloch sphere for the same parameters. Here the mapping from the BZ covers the Bloch sphere just once with the center of the zone mapping to the top of the sphere and the four equivalent points at the corners of the BZ mapping to the bottom. Since the band structure is fully gapped and the map in (c) covers the Bloch sphere, we expect that this band structure will yield a topological insulator when filled with fermions with Fermi energy residing in the gap. This is confirmed in (d) by the Chern number computed in the lowest band using Eq. (1). The red lines indicate parameter values at which the band gap closes. As expected, these are the only places where C changes.

where $\check{\sigma}$ and $\check{1}$ are the vector of Pauli matrices and the identity, respectively; summation over repeated indices is implied. Furthermore, $\mathbf{\Omega}(\mathbf{q}) = \mathbf{\Omega}(\mathbf{q} + q_r \mathbf{e}_x) = \mathbf{\Omega}(\mathbf{q} + q_r \mathbf{e}_y)$ defines the spin-dependent eigenstates comprising the lowest two Brillouin zones (BZs); q_r is the reciprocal lattice wave vector; $\hat{\phi}_m^\dagger(\mathbf{q})$ describes the creation of a particle with crystal momentum \mathbf{q} in the m th spin state; and we define $\mathbf{\Omega}(\mathbf{q}) \cdot \mathbf{\Omega}(\mathbf{q}) \equiv \Omega(\mathbf{q})^2$. This system is described by a pair of energy bands, at each \mathbf{q} separated in energy by $\Omega(\mathbf{q})$, with spin- and momentum-dependent eigenstates parallel to $\mathbf{\Omega}(\mathbf{q})$ on the Bloch sphere. In terms of the normalized vector $\mathbf{n}(\mathbf{q}) = \mathbf{\Omega}(\mathbf{q})/\Omega(\mathbf{q})$, the Chern number (the suitable topological invariant for this system)

$$C_{\pm} = \pm \frac{1}{4\pi} \int_{\text{BZ}} \mathbf{n}(\mathbf{q}) \cdot \left[\frac{\partial \mathbf{n}(\mathbf{q})}{\partial q_x} \times \frac{\partial \mathbf{n}(\mathbf{q})}{\partial q_y} \right] \quad (1)$$

is equal and opposite for the two bands, and counts the number of times the Bloch sphere is covered in the integration over the BZ. Direct measurement of this quantity is challenging.

Simple model. With this context, consider the spin-dependent band structure defined by

$$\mathbf{\Omega}(\mathbf{q}) = \Omega_{\perp} [\sin(q_x) \mathbf{e}_x + \sin(q_y) \mathbf{e}_y] + \{\Omega_{\text{RF}} + \Omega_{\parallel} [\cos(q_x) + \cos(q_y)] \mathbf{e}_z\}, \quad (2)$$

where we have taken the reciprocal lattice wave vector to be $q_r = 2\pi$, implying the lowest BZ extends from $-\pi$ to π along both \mathbf{e}_x and \mathbf{e}_y . Figure 1a shows that the map from the BZ to the Bloch sphere in Eq. (2) covers the sphere once, suggesting that the resulting band structure is topologically non-trivial with Chern numbers $C = \pm 1$ in the lowest two bands.

Because Eq. (2) includes only 0 and $\pm q_r$ momentum components, the Hamiltonian's coordinate space representation (for $\Omega_{\parallel} = \Omega_{\perp} = \Omega_{\text{RF}} \equiv \Omega_0$)

$$\begin{aligned} \hat{\mathcal{H}} = & - \sum_{i,j} \left\{ \hat{\mathbf{a}}_{i+1,j}^\dagger \check{t}_x \hat{\mathbf{a}}_{i,j} + \hat{\mathbf{a}}_{i,j+1}^\dagger \check{t}_y \hat{\mathbf{a}}_{i,j} + \text{HC} \right\} \\ & + \frac{\Omega_0}{2} \sum_{i,j} \hat{\mathbf{a}}_{i,j}^\dagger \check{\sigma}_z \hat{\mathbf{a}}_{i,j}, \end{aligned} \quad (3)$$

with

$$\check{t}_{x,y} = -\frac{\Omega_0}{4} [e^{i\pi/2} \check{\sigma}_{x,y} + \check{\sigma}_z],$$

requires simple nearest-neighbor – though spin-dependent – hopping, along with a local Zeeman shift. Here $\hat{\mathbf{a}}_{i,j}^\dagger$ is a two-component field operator describing the creation of a particle at site (i, j) . Extensions of the initial Jaksch and Zoller proposal for creating artificial abelian magnetic fields [17] using light- or radiofrequency-induced spin-dependent hopping can lead to Hamiltonians of this type [18]; indeed, Eq. (3) is a minimal case of the proposal previously [19, 20]. In an experimental realization, all hopping – between nearest neighbors of a spin-dependent bipartite lattice – would be generated by external control fields: Ω_\parallel and Ω_\perp would be induced by light-induced hopping, while Ω_{RF} would be generated by a uniform radiofrequency coupling.

Figure 1a shows schematically the geometry of this lattice, where induced hopping along \mathbf{e}_x or \mathbf{e}_y couples together sites of a bipartite lattice. This can generate tunable spin-dependent hopping matrix elements \check{t}_x and \check{t}_y , dependent on the phase, direction, and strength of the Raman lasers driving the hopping.

Chern number detection. With ultracold atoms in optical lattices, it is straightforward to measure the momentum distribution $\rho(\mathbf{k})$, where $\mathbf{p} = \hbar\mathbf{k}$ is the momentum, by abruptly removing the lattice and trapping potentials, allowing the atomic ensemble to expand in the absence of interactions for a sufficiently long time-of-flight (TOF) period [21], followed by absorption imaging. For deep lattices, when the tight-binding approximation is valid, we have

$$\rho(\mathbf{k}) = |\tilde{w}(\mathbf{k})|^2 \rho_{\text{cry}}(\mathbf{k}) = |\tilde{w}(\mathbf{k})|^2 \sum_{j,l} e^{i\mathbf{k} \cdot (\mathbf{j}-\mathbf{l})} \langle \Psi | \hat{a}_j^\dagger \hat{a}_l | \Psi \rangle, \quad (4)$$

where $\tilde{w}(\mathbf{k})$ is the Fourier transform of the localized Wannier function $w(\mathbf{r})$ describing atoms localized in individual lattice sites and $\rho_{\text{cry}}(\mathbf{q}) = \langle \hat{\phi}^\dagger(\mathbf{q}) \hat{\phi}(\mathbf{q}) \rangle$ is the crystal momentum distribution.

The crystal momentum distribution can be experimentally measured using band mapping techniques [22, 23], where the optical lattice potential is ramped off as adiabatically as possible just before TOF. Unfortunately, these techniques are plagued with unavoidable failures of adiabaticity near the BZ edges, or more generally, wherever the band gap closes. Equation (4) shows that the crystal momentum can be measured more directly, simply using $\rho_{\text{cry}}(\mathbf{k}) = \rho(\mathbf{k}) / \tilde{w}(\mathbf{k})$, with \mathbf{k} confined to the lowest BZ where $\tilde{w}(\mathbf{k})$ is not small (experimentally, better results can be obtained by averaging over all

\mathbf{k} , suitably weighted to account for technical noise [24]). Relevant here, the spin-resolved momentum distribution can be obtained by introducing a magnetic field gradient during TOF to Stern–Gerlach separate the two spin components, $\rho_{\text{cry},\uparrow}(\mathbf{q})$ and $\rho_{\text{cry},\downarrow}(\mathbf{q})$, with the normalized difference yielding the \mathbf{e}_z component of the magnetization

$$m_z(\mathbf{q}) = \frac{\rho_{\text{cry},\uparrow}(\mathbf{q}) - \rho_{\text{cry},\downarrow}(\mathbf{q})}{\rho_{\text{cry},\uparrow}(\mathbf{q}) + \rho_{\text{cry},\downarrow}(\mathbf{q})}.$$

In this setting, the power of cold atom experiments is evident: simple $\pm\pi/2$ rotations about either \mathbf{e}_x or \mathbf{e}_y just before TOF transform the $m_y(\mathbf{q})$ or $m_x(\mathbf{q})$ observable into $m_z(\mathbf{q})$. Sau *et al.* [25] noted that a band insulator – or any state where each momentum state in the lowest band is occupied with equal probability – allows the full magnetization vector $\mathbf{M}(\mathbf{q}) = -\mathbf{n}(\mathbf{q})$ to be obtained with just three measurements. Thus, the Chern number can be obtained directly by integrating experimental data [26].

Figure 2a depicts simulated spin-resolved momentum distributions including realistic technical noise, and Fig. 2b shows the resulting three components of $\mathbf{M}(\mathbf{q})$. From the three magnetization components, the Chern number can be directly computed by applying a discretized version of Eq. (1), leading to the Chern numbers displayed in Fig. 2c at zero temperature and in Fig. 2d at $k_B T = \Omega_\perp$. In both cases, the topological phase diagram displayed in Fig. 1d is clearly reproduced.

In many cases, the flatness of the band structure matters; for example, fractional quantum Hall effects (FQHEs) require that the band width be small compared to the typical interaction strength. As Yang *et al.* [27] show, it is possible to produce arbitrarily flat bands (also with arbitrary Chern number) by systematically including long-range (spin-dependent) hopping terms into the Hamiltonian. To understand this, again consider $\Omega(\mathbf{q})$ from Eq. (2) with $\Omega_0 = \Omega_\parallel = \Omega_\perp = \Omega_{\text{RF}}$, giving

$$\Omega(\mathbf{q}) = \Omega_0 \sqrt{5(1 + \alpha)}, \quad \text{with}$$

$$\alpha = \frac{1}{5} [\cos(q_x) + \cos(q_y) + \cos(q_x) \cos(q_y) - 1].$$

Using the normalized vector $\mathbf{n}(\mathbf{q}) = \Omega(\mathbf{q}) / \Omega(\mathbf{q})$, a new coupling $\Omega'(\mathbf{q}) = \Omega_0 \mathbf{n}(\mathbf{q})$ gives rise to flat bands, gapped by Ω_0 and with C_\pm unchanged. This can be approximated order-by-order in powers α , giving spin-dependent hopping of arbitrary range. This type of engineering is in principle elegant, but even next-nearest-neighbor tunneling is difficult to engineer at will.

Flux lattices, as invented by Cooper and Dalibard [28], provide a direct pathway for engineering topological band structures (also see earlier work [29] invoking

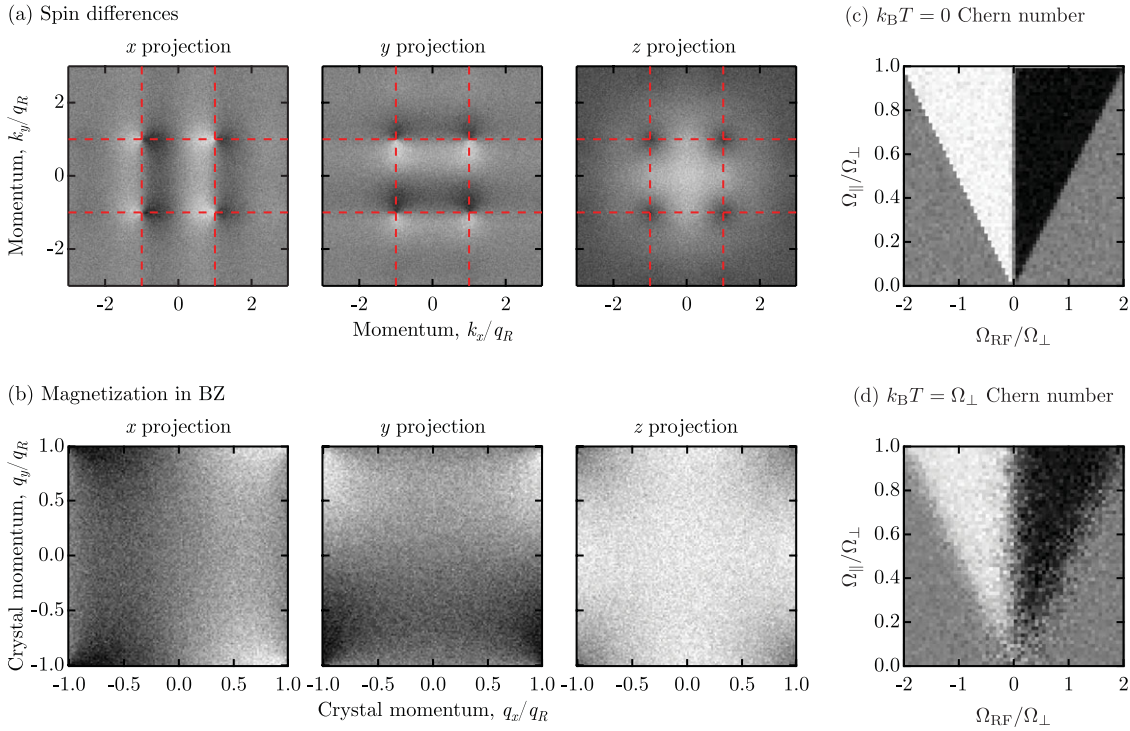


Figure 2 Simulated experiment. (a) Simulated spin-difference momentum distributions of non-interacting $T = 0$ fermions with E_F in the band gap and $\Omega_0 = \Omega_{\parallel} = \Omega_{\perp} = \Omega_{\text{RF}}$, including realistic noise from photon and atom shot noise. The dashed lines mark the edge of the BZ. (b) Magnetization components extracted from the data in (a). Chern number directly computed from such images as a function of tunable parameters at (c) $T = 0$ and (d) $k_B T = \Omega_{\perp}$.

the same concept using magnetic coupling). While the systematic band-flattening procedure of Ref. [27] cannot be applied without additional lasers, the large number of parameters in flux-lattice configurations [30] in principle allow for the formation of nearly perfectly flat bands [31, 32] without additional experimental complexity. These conceptually simple lattice structures require as few as four laser fields, Raman-coupling together different internal atomic states.

4 Edge states

The Chern number C_n of the n th band is a non-local measure of the eigenstate topology within that band. A remarkable result by Thouless, Kohmoto, Nightingale, and den Nijs [5] – the celebrated TKNN formula – showed that the Hall conductivity of a Chern insulator is given by

$$\sigma_{xy} = \frac{h}{e} \sum_n C_n, \quad (5)$$

the sum of the Chern numbers of all bands below the Fermi energy. This simple observation connects topol-

ogy inside a gapped insulator to the properties of its edge states, and explains the quantized Hall conductivity in both the IQHE [33] and the FQHE [34]. In addition to the direct measurement of topological indices discussed above, cold atom systems allow for measurement of edge state transport [35]. Here I illustrate the sharp contrast between edge and transport that can be observed in cold atom systems, by focusing on the type of artificial gauge fields already realized in the laboratory [36].

Many of the initial proposals for creating artificial gauge fields without optical lattices [37–39] – as realized at NIST/JQI [36] – create a synthetic magnetic field in a region of space bounded in one direction, here \mathbf{e}_y . With these experimental techniques, the unavoidable inhomogeneity makes a direct connection to topological invariants difficult. As I show below, these systems, with their natural boundaries, can be bulk insulators with chiral edge states, allowing a direct application of the TKNN formula.

Most studies of artificial gauge fields (see, for example, the outstanding review article by Dalibard *et al.* [11]) consider the properties of laser-dressed atoms moving adiabatically in just one “dressed” state. In this dressed state, Berry’s phase effects can give rise to synthetic

gauge fields. In what follows, I study (1) the adiabatic gauge field [11]; then (2) relax the adiabatic approximation somewhat [39]; (3) solve for the full eigenstate structure suitable for the NIST/JQI experiments without any adiabatic approximation; (4) show the system is a bulk insulator; and (5) identify the chiral edge states. This discussion follows the presentation first put forth in the methods of Beeler *et al.* [40].

Review of IQHE systems. Before discussing artificial gauge fields, consider the more commonplace problem of fermions with charge e moving in 2D, subject to a perpendicular magnetic field $\mathbf{B} = -B\mathbf{e}_z$, confined in a box potential

$$V_{\text{box}}(y) = \begin{cases} 0 & \text{for } y \in (-L_y/2, L_y/2) \\ \infty & \text{otherwise} \end{cases}$$

along \mathbf{e}_y . This system, with single particle states described by the Landau gauge Hamiltonian

$$\hat{H} = \frac{\hbar^2}{2m} \left(\hat{\mathbf{k}} - \frac{eBy}{\hbar} \mathbf{e}_x \right)^2 + V_{\text{box}}(y),$$

can be directly solved by taking the ansatz $\psi(x, y) = \exp(iqx) f_q(y)$ for the eigenfunctions. This gives the one-dimensional (1D) Schrödinger equation

$$E_q f_q(y) = \left[-\frac{\hbar^2}{2m} \frac{\partial^2}{\partial y^2} + \frac{1}{2} m \Omega_c^2 (y - \ell_B^2 q)^2 + V_{\text{box}}(y) \right] f_q(y)$$

for $f_q(y)$; q , the plane-wave wave vector along \mathbf{e}_x , should be interpreted as being somewhat like a canonical momentum (and definitely not a mechanical momentum); $\ell_B = \sqrt{\hbar/eB}$ is the magnetic length; and $\Omega_c = eB/m$ is the cyclotron frequency. When $V_{\text{box}}(y)$ is absent, this gives harmonic oscillator solutions for $f_q(y)$ labeled by the Landau level index n , spaced in energy by $\hbar\Omega_c$, centered at $y_0 = \ell_B^2 q$, and with oscillator width ℓ_B .

When $V_{\text{box}}(y) \neq 0$, the eigenenergies remain close to the homogeneous system values provided y_0 is more than $\sim \ell_B$ from the boundaries. But as Fig. 3a shows, the energies rapidly increase as $|\ell_B^2 q|$ exceeds $L_y/2$ and the wave function is pressed against the system's walls. Here, we see that for any given Fermi energy (depicted for example in the bulk gap between the $n = 0$ and $n = 1$ Landau levels), states – one pair per Landau level – reside at the Fermi energy (two states in the pictured case) and the only low-energy excitations are near these edge states. In this geometry, these are the edge states predicted by the TKNN formula, each contributing a single quantum of conductance. We explicitly verify this interpretation in

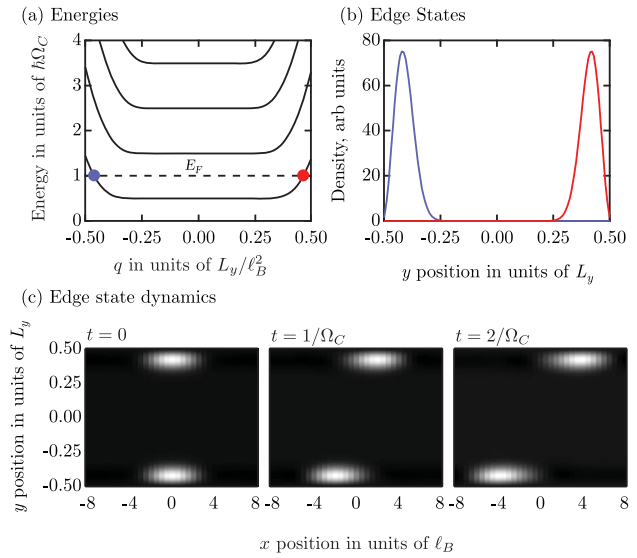


Figure 3 Quantum Hall edge states computed for $L_y = 2\pi\ell_B$ and positive charge. (a) Energy as a function of q . In the bulk, this defines the $y_0 = q\ell_B^2$ center position. (b) Edge state density distributions at the two points marked in (a) at the Fermi energy. (c) Time evolution of a density perturbation created by the potential $V'(x) = V_0 \exp[-(x/\ell_B)^2]$, with $V_0 = -\hbar\Omega_c/40$ which is removed at $t = 0$, showing that the excitation propagates in a chiral manner and only at the edges.

two ways. Firstly, Fig. 3b plots the electron density associated with these two edge states, showing that they reside at the system's edge. Secondly, Fig. 3c shows the time evolution of a numerical experiment where a weak attractive Gaussian potential centered at $x = 0$ and extended along y is removed at $t = 0$. At $t = 0$ (left-hand panel of Fig. 3c), we see localized regions of increased electron density at the system's edges, reflecting the incompressible bulk. As t increases, this density perturbation propagates in a chiral manner on the top and bottom edges, with group velocity simply given by $v_g = \hbar^{-1} \partial_q E_0(q)$. This same method of solution can be applied in the symmetric gauge case for the disk geometry (suitable for the first continuum gauge field proposals [37]).

Artificial gauge fields: adiabatic picture. Figure 4a shows the typical laser geometry and coupling scheme for the three-level case realized in experiment. In the temporally rotating frame with the rotating wave approximation, and after a suitable gauge transformation, this system is described by the single-particle Hamiltonian (see Ref. [30] for a first-principles derivation)

$$\tilde{H} = \frac{\hbar^2}{2m} \left(\hat{\mathbf{k}} - \frac{2k_R \tilde{F}_z}{\hbar} \mathbf{e}_x \right)^2 + \Omega'_R \tilde{F}_x + \delta(\hat{y}) \tilde{F}_z + V_{\text{tot}}(\hat{y}) \quad (6)$$

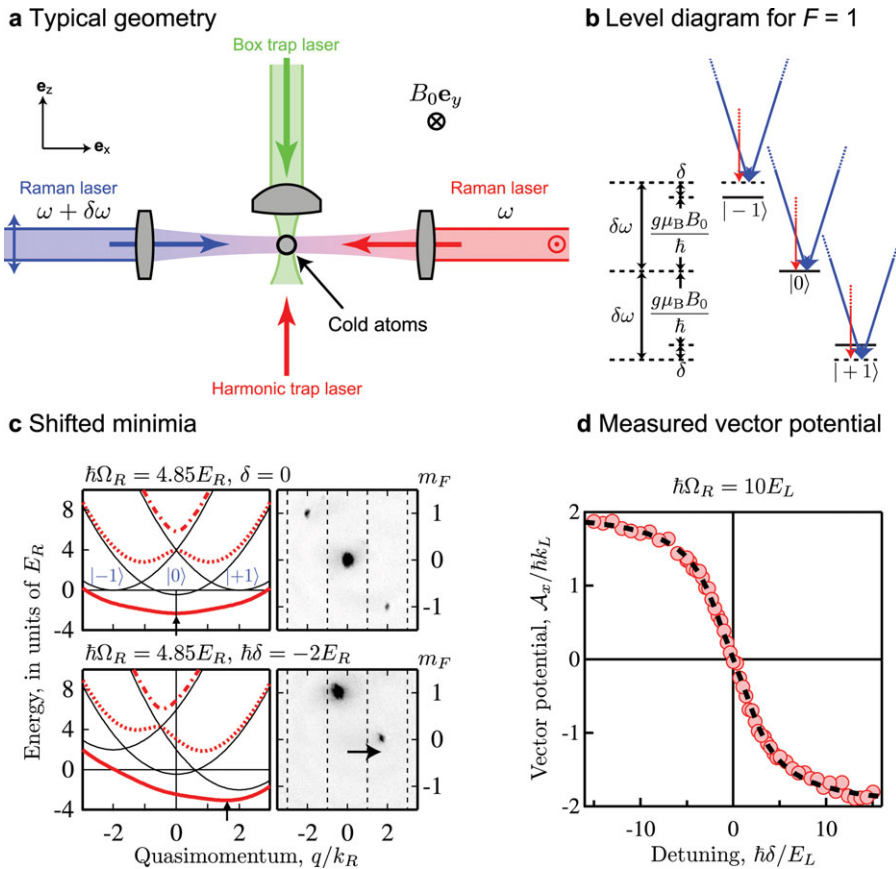


Figure 4 Typical two-beam experimental geometry. (a) Side view of laser geometry including Raman laser beams with wavelength λ (≈ 790 nm for ^{87}Rb). For the edge state calculation, a $\lambda \approx 1064$ nm laser provides a harmonic confining potential along \mathbf{e}_x and a $\lambda = 532$ nm laser generates a box potential along \mathbf{e}_y . (b) Physical level diagram for three-level total angular momentum $f = 1$ case, as is applicable for the common alkali metal atoms ^7Li , ^{23}Na , ^{39}K , ^{41}K , and ^{87}Rb . The generally small quadratic Zeeman effect that makes the $| -1\rangle \rightarrow |0\rangle$ energy difference different from that of $|0\rangle \rightarrow | +1\rangle$ is not included in this diagram. (c) Computed dispersion relations (left-hand panels), with: $\mathcal{E}_-(q\mathbf{e}_x, \Omega_R, \delta)$, red solid; $\mathcal{E}_0(q\mathbf{e}_x, \Omega_R, \delta)$, red dotted; and $\mathcal{E}_+(q\mathbf{e}_x, \Omega_R, \delta)$, red dash-dot. In addition, the solid curves depict bare states. The vertical arrow locates the minimum of the lowest energy dressed curve. Right-hand panels: representative images of Raman-dressed atoms both on and off of resonance showing the three m_F components differing in momentum by $\pm 2\hbar k_R$, displaced from zero q when $\delta \neq 0$. The horizontal arrow depicts the displacement of the $m_F = 0$ cloud from zero corresponding to the non-zero vector potential. (d) Measured momentum of $m_F = 0$ component as a function of detuning δ . With the gauge choice $\mathcal{A}(\delta = 0) = 0$, this constitutes a direct measurement of the artificial vector potential $\mathcal{A}(\delta)$. The dashed curve is the predicted vector potential for the experimental parameters. Data first appeared in Lin *et al.*, Phys. Rev. Lett. **102**, 130401 (2009) [41] and Lin *et al.*, Nat. Phys. **7**, 531 (2011) [42].

for an atom with total angular momentum f in the \mathbf{e}_x – \mathbf{e}_y plane. $\hat{F}_{x,y,z}$ are the total angular momentum operators; $p_R = \hbar k_R$ and $E_R = \hbar^2 k_R^2 / 2m$ are the single-photon recoil momentum and energy; Ω_R is the Raman coupling strength; $\delta(y)$ is a position-dependent detuning from Raman resonance; and $V_{\text{tot}}(y)$ is an external confining potential. In the various adiabatic approximations, Eq. (6) is solved, for example ignoring the spatial dependence of δ , giving a set of dressed states that contain a

vector potential term that depends parametrically on δ and Ω'_R .

First, we can anticipate that this Hamiltonian might give rise to effective magnetic fields by assuming that $\sqrt{q(\Omega'_R)^2 + \delta(y)^2}$ is large compared to the kinetic energy, and so that motion is fully adiabatic within the resulting dressed states. This is solved by rotating $\hat{\mathbf{F}}$ about \hat{F}_y by an angle given by $\tan \theta = \Omega'_R / \delta(y)$; the dynamics in any given band labeled by m_F is governed by the projected

Hamiltonian

$$\hat{H} = \frac{\hbar^2}{2m} \left[\hat{k} - \frac{\mathcal{A}(\mathbf{r})}{\hbar} \right]^2 + V(\mathbf{r}) + W(\mathbf{r}). \quad (7)$$

Using the formalisms of Dalibard *et al.* [11] (in terms of wave functions) or Madison *et al.* [13] (in terms of unitary transformations), it is straightforward to show that each of these bands independently has a vector potential

$$\mathcal{A}(\mathbf{r}) = 2\hbar k_R m_F \left[\frac{\delta}{\sqrt{\delta^2 + (\Omega'_R)^2}} \right] \mathbf{e}_x, \quad (8)$$

along with adiabatic and geometric potentials

$$V(\mathbf{r}) = \hbar m_F \sqrt{(\Omega'_R)^2 + \delta^2}$$

$$W(\mathbf{r}) = \frac{\hbar^2 k_R^2 (\Omega'_R)^2}{m [\delta^2 + (\Omega'_R)^2]} [f(f+1) - m_F^2]. \quad (9)$$

Typically experiments are performed in the lowest energy dressed state, where $m_F = -f$ assumes its maximal magnitude. Equation (8) illustrates two important points: firstly, that the magnitude $\mathcal{A}_{m_F}(\mathbf{r})$ is defined by the recoil momentum of the lasers as well as m_F ; and secondly, that the vector potential is strictly bounded between $\pm 2\hbar k_R m_F$. Suppose now that the vector potential $\mathcal{A}(\mathbf{r}) \propto \mathbf{e}_x$ depends on y , for example via a linear detuning gradient: this would result in a Landau gauge form vector potential with non-zero synthetic magnetic field [38, 39]. Thus the adiabatic approximation – if it should be trusted – leads us to expect a magnetic field (observed in Ref. [36]) in this geometry.

This kind of adiabatic approximation is far stronger than needed. A weaker adiabatic approximation takes the explicit matrix

$$\check{H}(\mathbf{q}) = \begin{pmatrix} \frac{\hbar^2(\mathbf{q}-2k_R\mathbf{e}_x)^2}{2m} + \hbar\delta & \frac{\hbar\Omega_R}{2} & 0 \\ \frac{\hbar\Omega_R}{2} & \frac{\hbar^2\mathbf{q}^2}{2m} + \epsilon & \frac{\hbar\Omega_R}{2} \\ 0 & \frac{\hbar\Omega_R}{2} & \frac{\hbar^2(\mathbf{q}+2k_R\mathbf{e}_x)^2}{2m} - \hbar\delta \end{pmatrix}$$

for Eq. (6), in this case for an $f = 1$ manifold, and exactly obtains its eigenvalues $\mathcal{E}_{\pm,0}(\mathbf{q}, \Omega_R, \delta)$. Here we introduced $\Omega_R = \Omega'_R/\sqrt{2}$, conforming to the notation of our earlier publications. Figure 4c shows these effective dispersion relations with minima shifted from zero (a vector potential, similar to the adiabatic result but quantitatively different) and with an effective mass larger than m (the effective mass is just m in the usual adiabatic approximation). Figure 4d then shows the experimentally measured synthetic vector potential, compared to theory.

Artificial gauge fields: numerically exact. Here we avoid adiabatic approximations altogether by solving the full Raman-coupled Hamiltonian for a system that is extended along \mathbf{e}_x ; has a detuning profile $\delta(y)$; and is confined in a potential $V_{\text{tot}}(y) = V_{\text{box}}(y) + V_{\text{comp}}(y)$ along \mathbf{e}_y . The compensation potential $V_{\text{comp}}(y)$ is described below and L_x and L_y describe the system's extent along \mathbf{e}_x and \mathbf{e}_y .

As with the solution of an electron moving in a uniform magnetic field expressed in the Landau gauge, this problem can be solved by taking a separable wave function of the form $\psi(x, y) = \exp(iqx)\chi_q(y)$. With this ansatz, the full 1D spinful, coordinate representation Hamiltonian describing motion along \mathbf{e}_y is

$$E_q \chi_q(y) = \left\{ \left[-\frac{\hbar^2}{2m} \frac{d^2}{dy^2} + \frac{\hbar^2 (q - 2k_R \tilde{F}_z)^2}{2m} + V_{\text{tot}}(y) \right] \tilde{\mathbb{I}} + \Omega'_R \tilde{F}_x + \delta(y) \tilde{F}_z \right\} \chi_q(y), \quad (10)$$

where $\chi_q(y)$ is a $2f+1$ component spinor wave function and $\tilde{\mathbb{I}}$ is the suitable identity. It is straightforward to numerically solve this 1D eigenvalue problem for any Ω'_R , $V_{\text{tot}}(y)$, and $\delta(y)$.

The scalar potentials $V(\mathbf{r})$ and $W(\mathbf{r})$ – which depend on δ – complicate matters. For the linear detuning gradient $\delta(y) = \delta'y$ we focus on, these can be well canceled by a Gaussian laser giving $V_{\text{comp}}(y)$: to have a bulk cyclotron gap, the residual potential modulations must be small compared to the effective cyclotron energy. Figure 4a depicts the complete required geometry including a blue-detuned beam creating a box-shaped trap potential along \mathbf{e}_y and an elliptical Gaussian beam, both providing compensation along \mathbf{e}_y and weak overall confinement along \mathbf{e}_x ; also, not pictured, is a 1D lattice along \mathbf{e}_z confining the system into 2D systems.

The four smallest eigenenergies of this Hamiltonian (Eq. (10)) are plotted as a function of q in Fig. 5a, showing that each state is specified by two quantum numbers: q and a Landau-level-like index n . We numerically verified that the low-energy spectra of this exact Hamiltonian (Eq. (10)) and that resulting from projecting onto the lowest band $\mathcal{E}_{\pm,0}(\mathbf{q}, \Omega_R, \delta)$ of Eq. (6) are indistinguishable. This is because atoms always reside near the local minima in $\mathcal{E}_-(q, \Omega_R, \delta)$. Near these minima, the band spacing $\mathcal{E}_+(q, \Omega_R, \delta) - \mathcal{E}_-(q, \Omega_R, \delta) > 4E_R$ is large compared to the $0.15E_R \approx h \times 500 \text{ Hz} = k_B \times 25 \text{ nK}$ interval between eigenenergies depicted in Fig. 5a (using ^{87}Rb parameters, the energy scale is twice as large as for ^{40}K). Figure 5a illustrates a second issue regarding this type of scheme: the vector potential saturates at $\pm 2\hbar k_R$ as $|\delta|$ becomes

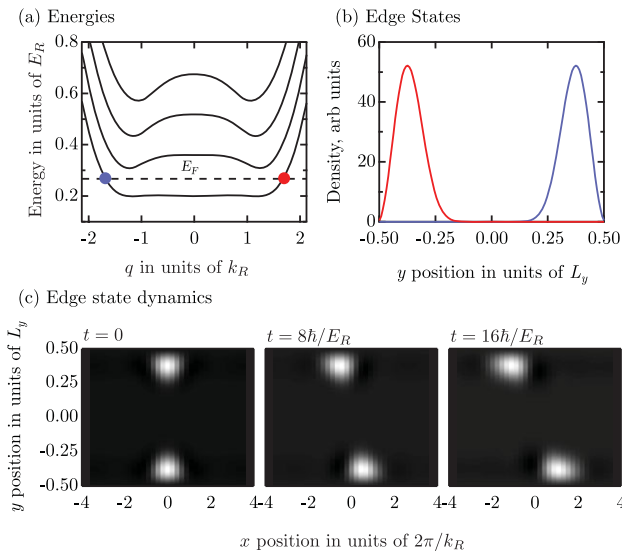


Figure 5 Synthetic quantum Hall edge states computed for $\Omega_R = 11 E_R$, with δ ranging from $-8 E_R$ to $8 E_R$ over the system's $L_y = 14\pi/k_R$ extent along \mathbf{e}_y . (a) Energy as a function of q . In the bulk, this is associated with the y_0 center position. (b) Edge state density distributions at the two points marked in (a) at the Fermi energy. (c) Time evolution of a density perturbation created by the potential $V'(x) = V_0 \exp[-(x/\ell_B)^2]$, with $V_0 = -E_R/300$ which is removed at $t = 0$, showing that the excitation propagates in a chiral manner and only at the edges.

large. As a result the magnetic field decreases to zero, and the cyclotron gap closes. The beginning of this effect is visible in Fig. 5a near $q = \pm 1.5 k_R$.

In systems of fermions with small Fermi energy E_F (horizontal line in Fig. 5a), the full QHE analogy is revealed: the two points at the Fermi energy correspond to edge modes on the top and bottom of the system. Figure 5b plots the computed density distribution of those eigenstates, showing that they reside on the system's edge, and in addition the two edge states counter-propagate (opposite group velocities).

Lastly, following the example of electrons in a magnetic field, we computed the time evolution of the system following the release of a small Gaussian potential perturbation $V'(x) = V_0 \exp[-(x/\ell_B)^2]$. Figure 5c shows the nearly non-dispersive motion of these states, counter-propagating on the two edges, with no visible perturbation in the bulk. Truly this system behaves as a quantum Hall system: application of the TKNN equation confirms the topological nature of these synthetic cyclotron bands.

Physical parameters. To estimate the number of fermionic ^{40}K atoms required, we consider a uniform sys-

tem with length L_x , constraining q to be a multiple of $\delta q = 2\pi/L_x$. Here the edge states are well isolated for a Fermi momentum $k_F \approx 2k_R = 4\pi/\lambda$ (solid red and blue circles in Fig. 5a). Since this energy is fully in the gap, it implies that states with $|q| \leq k_F$ are occupied. Thus, the number of states below the Fermi energy is $N_F = 4L_x/\lambda$. For example, when $L_x = 50\lambda$ the number of atoms will be $N_F = 200$, and the proposed system with height $L_y = 7\lambda$ has a reasonable aspect ratio. With these approximately 200 atoms, the Fermi energy will lie in the gap between the $N = 0$ and $N = 1$ bands, which are spaced by $\approx 1000 \text{ Hz} \approx 50 \text{ nK}$. As with existing proposals for creating topological matter with cold atoms [17–19, 28, 31, 43–46], the required energy scales and atom numbers are low, but within the scales that have already been realized in the laboratory [8, 47]. In this case, to identify the existence of edge states, the recent technique proposed by Goldman *et al.* [35] could be implemented to directly image the motion of edge states, more dramatically than what is shown in Fig. 5c.

The conceptually simple method for designing the vector potential discussed here relies on only two lasers and three atomic states, making the experimental implementation relatively easy. One of the major stumbling blocks in using alkali metal atoms for QHE physics is the large photon scattering rate from the Raman lasers for alkali metal fermions, which leads to significant heating of the sample [19]. It is an ongoing research project to create schemes that are simple, have low spontaneous emission, and have unbounded vector potentials.

5 Conclusions

In this tutorial article, I have discussed two complementary methods by which a topological invariant – the Chern number – can be measured, either directly in terms of its definition or indirectly via edge-state transport using many-atom systems near thermodynamic equilibrium. These approaches – well defined in the context of the simple single-particle physics underlying topological insulators – give the basic context in which new methods, applicable for interacting systems such as p -wave superconductors or FQHEs, can be invented and implemented. For example, as coherent and isolated quantum systems, ultracold atoms are ideally placed to perform interference experiments – with bosons or fermions – both building on the ideas from quantum Hall systems (such as quasi-particle interferometers [48]) and also going in new directions (such as the recent experimental measurement of the Zak phase in a 1D

ladder-type system [49]). An alternative promising dynamical technique is to look at the gauge field's effect on Bloch oscillations [50].

Key words. Artificial gauge fields, spin-orbit coupling, quantum gases, Raman coupling, topological matter, edge states, chern numbers.



Ian B. Spielman received his Ph.D. degree in physics from the California Institute of Technology in 2004 for studying quantum Hall bilayers. As a postdoc he spent two years at NIST, Gaithersburg (USA) studying the physics of the superfluid-to-insulator transition in 2D atomic Bose gases.

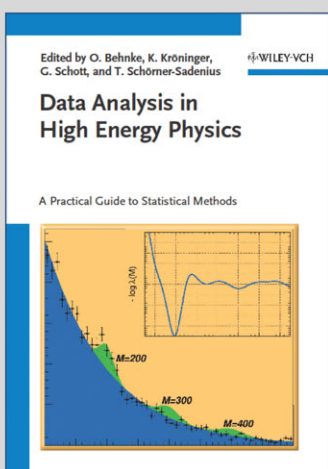
Since 2006 he is a physicist at NIST. His research focuses on realizing Hamiltonians familiar in condensed matter physics in atomic systems, including pioneering work creating artificial gauge fields for neutral atoms.

References

- [1] C. Shull, W. Strauser, and E. Wollan, *Phys. Rev.* **83**, 333 (1951).
- [2] D. Osheroff, R. Richardson, and D. Lee, *Phys. Rev. Lett.* **28**, 885 (1972).
- [3] R. Balian and N. Werthamer, *Phys. Rev.* **131**, 1553 (1963).
- [4] K. von Klitzing, *Rev. Mod. Phys.* **58**, 519 (1986).
- [5] D. J. Thouless, M. Kohmoto, M. P. Nightingale, and M. den Nijs, *Phys. Rev. Lett.* **49**, 405 (1982).
- [6] A. P. Schnyder, S. Ryu, A. Furusaki, and A. W. W. Ludwig, *Phys. Rev. B* **78**, 195125 (2008).
- [7] C. L. Kane and E. J. Mele, *Phys. Rev. Lett.* **95**, 146802 (2005).
- [8] F. Serwane, G. Zürn, T. Lompe, T. B. Ottenstein, A. N. Wenz, and S. Jochim, *Science* **332**, 336 (2011).
- [9] K. M. R. van der Stam, E. D. van Ooijen, R. Meppelink, J. M. Vogels, and P. van der Straten, *Rev. Sci. Instrum.* **78**, 013102 (2007).
- [10] V. Galitski and I. B. Spielman, *Nature* **494**, 49 (2013).
- [11] J. Dalibard, F. Gerbier, G. Juzeliūnas, and P. Öhberg, *Rev. Mod. Phys.* **83**, 1523 (2011).
- [12] H. Zhai, *Int. J. Mod. Phys. B* **26**, 1230001 (2012).
- [13] K. W. Madison, Y. Wang, A. M. Rey, and K. Bongs (eds.), *Annual Review of Cold Atoms, and Molecules*, Vol. 1 World Scientific, Singapore, (2013).
- [14] I. H. Deutsch and P. S. Jessen, *Phys. Rev. A* **57**, 1972 (1998).
- [15] A. M. Dudarev, R. B. Diener, I. Carusotto, and Q. Niu, *Phys. Rev. Lett.* **92**, 153005 (2004).
- [16] J. Sebby-Strabley, M. Anderlini, P. S. Jessen, and J. V. Porto, *Phys. Rev. A* **73**, 033605 (2006).
- [17] D. Jaksch and P. Zoller, *New J. Phys.* **5**, 56 (2003).
- [18] K. Osterloh, M. Baig, L. Santos, P. Zoller, and M. Lewenstein, *Phys. Rev. Lett.* **95**, 010403 (2005).
- [19] N. Goldman, I. Satija, P. Nikolic, A. Bermudez, M. A. Martin-Delgado, M. Lewenstein, and I. B. Spielman, *Phys. Rev. Lett.* **105**, 255302 (2010).
- [20] N. Goldman, F. Gerbier, and M. Lewenstein, *arxiv*: 1301.4959 (2013).
- [21] M. Greiner, O. Mandel, T. Esslinger, T. Hänsch, and I. Bloch, *Nature* **415**, 39 (2002).
- [22] D. McKay, M. White, and B. DeMarco, *Phys. Rev. A* **79**, 063605 (2009).
- [23] S. S. Natu, D. C. McKay, B. DeMarco, and E. J. Mueller, *Phys. Rev. A* **85**, 061601 (2012).
- [24] I. B. Spielman, W. D. Phillips, and J. V. Porto, *Phys. Rev. Lett.* **98**, 080404 (2007).
- [25] J. D. Sau, R. Sensarma, S. Powell, I. B. Spielman, and S. Das Sarma, *Phys. Rev. B* **83**, 140510 (2011).
- [26] E. Alba, X. Fernandez-Gonzalvo, J. Mur-Petit, J. Pachos, and J. Garcia-Ripoll, *Phys. Rev. Lett.* **107**, 235301 (2011).
- [27] S. Yang, Z. C. Gu, K. Sun, and S. Das Sarma, *Phys. Rev. B* **86**, 241112(R) (2012).
- [28] N. R. Cooper and J. Dalibard, *Europhys. Lett.* **95**, 66004 (2011).
- [29] M. Taillefumier, E. K. Dahl, A. Brataas, and W. Hofstetter, *Phys. Rev. B* **80**, 020407(R) (2009).
- [30] G. Juzeliūnas and I. B. Spielman, *New J. Phys.* **14**, 123022 (2012).
- [31] N. R. Cooper, *Phys. Rev. Lett.* **106**, 175301 (2011).
- [32] N. R. Cooper and R. Moessner, *Phys. Rev. Lett.* **109**, 265301 (2012).
- [33] K. von Klitzing, G. Dorda, and M. Pepper, *Phys. Rev. Lett.* **45**, 494 (1980).
- [34] D. C. Tsui, H. L. Stormer, and A. C. Gossard, *Phys. Rev. Lett.* **48**, 1559 (1982).
- [35] N. Goldman, J. Dalibard, A. Dauphin, F. Gerbier, M. Lewenstein, P. Zoller, and I. B. Spielman, "Direct imaging of topological edge states in cold-atom systems", in: *Proceedings of the National Academy of Sciences of the United States of America* **110**, 6736–6741 (2013).
- [36] Y. J. Lin, R. L. Compton, K. Jimenez-Garcia, J. V. Porto, and I. B. Spielman, *Nature* **462**, 628 (2009).
- [37] G. Juzeliūnas, P. Öhberg, J. Ruseckas, and A. Klein, *Phys. Rev. A* **71**, 053614 (2005).
- [38] G. Juzeliūnas, J. Ruseckas, P. Öhberg, and M. Fleischhauer, *Phys. Rev. A* **73**, 025602 (2006).
- [39] I. B. Spielman, *Phys. Rev. A* **79**, 063613 (2009).
- [40] M. C. Beeler, R. A. Williams, K. Jiménez-García, L. J. LeBlanc, A. R. Perry, and I. B. Spielman, *Nature* **498**, 201–204 (2013).

- [41] Y. J. Lin, R. L. Compton, A. R. Perry, W. D. Phillips, J. V. Porto, and I. B. Spielman, *Phys. Rev. Lett.* **102**, 130401 (2009).
- [42] Y. J. Lin, R. L. Compton, K. Jimenez-Garcia, W. D. Phillips, J. V. Porto, and I. B. Spielman, *Nat. Phys.* **7**, 531 (2011).
- [43] J. Ruseckas, G. Juzeliunas, P. Ohberg, and M. Fleischhauer, *Phys. Rev. Lett.* **95**, 010404 (2005).
- [44] K. J. Günter, M. Cheneau, T. Yefsah, S. P. Rath, and J. Dalibard, *Phys. Rev. A* **79**, 011604 (2009).
- [45] P. Hauke, O. Tieleman, A. Celi, C. Ölschläger, J. Simonet, J. Struck, M. Weinberg, P. Windpassinger, K. Sengstock, M. Lewenstein, and A. Eckardt, *Phys. Rev. Lett.* **109**, 145301 (2012).
- [46] L. J. Lang, X. Cai, and S. Chen, *Phys. Rev. Lett.* **108**, 220401 (2012).
- [47] R. Joerdens, N. Strohmaier, K. Guenther, H. Moritz, and T. Esslinger, *Nature* **455**, 204 (2008).
- [48] C. Nayak, S. H. Simon, A. Stern, M. Freedman, and S. D. Sarma, *Rev. Mod. Phys.* **80**, 1083 (2008).
- [49] M. Atala, M. Aidelsburger, J. T. Barreiro, D. Abanin, T. Kitagawa, E. Demler, and I. Bloch, *arxiv:1212.0572* (2012).
- [50] H. M. Price and N. R. Cooper, *Phys. Rev. A* **85**, 033620 (2012).

+++ NEW +++ NEW +++ NEW +++ NEW +++ NEW +++ NEW +++ NEW +++



2013. 440 Pages, Softcover
150 Fig.
ISBN 978-3-527-41058-3

OLAF BEHNKE / KEVIN KRÖNINGER / GRÉGORY SCHOTT / THOMAS
SCHÖRNER-SADENIUS (EDS.)

Data Analysis in High Energy Physics

A Practical Guide to Statistical Methods

This practical guide covers the essential tasks in statistical data analysis encountered in high energy physics and provides comprehensive advice for typical questions and problems. The basic methods for inferring results from data are presented as well as tools for advanced tasks such as improving the signal-to-background ratio, correcting detector effects, determining systematics and many others. Concrete applications are discussed in

analysis walkthroughs. Each chapter is supplemented by numerous examples and exercises and by a list of literature and relevant links. The book targets a broad readership at all career levels - from students to senior researchers. An accompanying website provides more algorithms as well as up-to-date information and links. Free solutions manual available for lecturers at www.wiley-vch.de/supplements/

Register now for the free
WILEY-VCH Newsletter!
www.wiley-vch.de/home/pas

WILEY-VCH • P.O. Box 10 11 61 • 69451 Weinheim, Germany
Fax: +49 (0) 62 01 - 60 61 84
e-mail: service@wiley-vch.de • <http://www.wiley-vch.de>

WILEY-VCH